A second-order coupled immersed boundary-SAMR construction for chemically reacting flow over a heat-conducting Cartesian grid-conforming solid

Kushal S. Kedia[a], Cosmin Safta[b], Jaideep Ray[b], Habib N. Najm[b], Ahmed F. Ghoniem[a*]

[a] *Department of Mechanical Engineering, Massachusetts Institute of Technology, Cambridge, MA, USA*

[b] *Sandia National Laboratories, Livermore, CA, USA*

Abstract

In this paper, we present a second-order numerical method for simulations of reacting flow around heat-conducting immersed solid objects. The method is coupled with a block-structured adaptive mesh refinement (SAMR) framework and a low-Mach number operator-split projection algorithm. A "buffer zone" methodology is introduced to impose the solid-fluid boundary conditions such that the solver uses symmetric derivatives and interpolation stencils throughout the interior of the numerical domain; irrespective of whether it describes fluid or solid cells. Solid cells are tracked using a binary marker function. The no-slip velocity boundary condition at the immersed wall is imposed using the staggered mesh. Near the immersed solid boundary, single-sided buffer zones (inside the solid) are created to resolve the species discontinuities, and dual buffer zones (inside and outside the solid) are created to capture the temperature gradient discontinuities. The development discussed

---

[*] Corresponding author

in this paper is limited to a two-dimensional Cartesian grid-conforming solid. We validate the code using benchmark simulations documented in the literature. We also demonstrate the overall second-order convergence of our numerical method. To demonstrate its capability, a reacting flow simulation of a methane/air premixed flame stabilized on a channel-confined bluff-body using a detailed chemical kinetics model is discussed.

Keywords: reacting flow, conjugate heat exchange, Cartesian solid, immersed boundary, adaptive mesh refinement, operator-split projection

---

1. Introduction

Combustors typically use flame-holders to provide the necessary mechanism for flame stabilization and continuous burning. There is often significant flame-wall interactions due to the conjugate heat exchange between the hot products and the nearby cooler flame-holder. In these systems, the length scales vary from the meter-scale combustor geometric details to the thin sub-millimeter-scale flame-fronts. The time scales span the slow conjugate heat exchange processes and the rapid diffusion and reaction phenomena. Our objective is to capture these wide spectra of spatial and temporal scales using an operator-split projection algorithm coupled with a block-structured adaptive mesh refinement (SAMR) framework and an immersed boundary formalism. When coupled with accurate flame-wall interaction treatment, fully resolved simulations can provide an insight into complex fundamental processes like flame stabilization, extinction and blow-off. Such simulations can also play a vital role in complementing experimental investigations of the detailed flame structure near the combustor walls; which is challenging due to the harsh environment, limited optical access and often inadequate field data.

Direct Numerical Simulations (DNS) involve solving the governing reacting flow equations on a computational grid that resolves all the relevant scales. Most DNS codes use fully explicit methods on a uniformly spaced or a stretched regular grid allowing simpler numerical implementation [1, 2]. This enables the use of high-order finite difference schemes to minimize numerical diffusion: fourth-order temporally accurate and eighth-order spatially accurate simulations were performed in [1, 2]. The stable time-step used in such codes is typically close to few nanoseconds for hydrocarbon combustion (4×10^{-9}s in [2]), primarily restricted by the stiffness of the chemical kinetics. A compressible flow construction, used in [2], imposes additional restriction on the stable time-step based on the sonic CFL condition. This extremely small time-stepping was significantly increased by constructing a low-Mach semi-implicit projection method, performing the transport and reactive time-advancement via specialized integrators [3, 4].

We investigated laminar flame stabilization, blow-off and resonant dynamics of premixed methane/air flames stabilized on heat-conducting perforated plate burners [5, 6] using the operator-split projection method described in [7] on a uniform structured grid. For such problems, where thin reaction fronts exist only in a small fraction of the computational domain, one may employ SAMR for higher efficiency. SAMR was first suggested by Berger and Oliger [8] and implemented for simulation of shock waves in [9]. Thereafter, it has been used in the simulation of flames with complex chemistry in a variety of laboratory configurations [10, 11]. Safta et al. [12] developed a spatially fourth-order and temporally second-order operator-split projection scheme for chemically reacting flows at the low-Mach number limit using the SAMR framework, which forms the basis of the current work.

The SAMR framework development for chemically reacting flows has hitherto been limited to fluid-only domains. Artificial flame anchoring conditions are often employed in the existing numerical simulations: a high temperature hot-spot in [2], isothermal flame-holder in [13] and hot combustion products co-flowing with the inflow reactants in [10]. As a result, DNS investigations are limited to the flow-field far away from the anchoring region. These artificial anchoring conditions are however advantageous because the slow time-scale of the conjugate heat exchange between the flame and burner wall is decoupled from the rapid combustion and flow time-scales. Gruber et al. [2] showed that incorporating heat exchange between isothermal (simplified model) channel walls and the interior reacting flow in a combustor was critical for accurate prediction of the high convective heat fluxes associated with the rapid radical quenching; however flame-wall interactions near the anchoring region were ignored. Accurate and efficient simulation tools to capture flame-wall interactions, allowing the flame to find a stable location naturally, are still unexplored and essential for understanding the localized phenomenon of flame stabilization. We addressed this issue in the context of low Reynolds number flow based perforated-plate burners in [5]. In that, we elucidated the flame stabilization mechanism highlighting the coupled role of curvature and local heat exchange with the burner. We also demonstrated that the conjugate heat exchange govern the unsteady response of premixed flames during flow perturbations in [6], which can be dangerous for an acoustically coupled combustor. Our objective here is to develop a coupled immersed boundary-SAMR approach allowing the flame to naturally stabilize near the flame-holder and accurately capture the flame-wall interactions.

Originally developed by Peskin [14] to simulate blood flow in the heart, the Immersed Boundary Method(IBM) has now found widespread use in a variety of engineering applications, although primarily limited to non reacting flows. The primary advantage of the IBM is that the non-grid conforming complex immersed bodies can be tackled on a regular Cartesian grid. Mittal and Iaccarino [15] presented a comprehensive review of the IBM. The presence of the solid body becomes known to the fluid through a forcing function, which is consistently constructed using the transport equations and the solid body constraint. Based on the method of forcing used, IBM can be categorized into a continuous forcing approach (forcing imposed in the governing equations before discretization) or a discrete forcing approach (forcing imposed in the governing equations after discretization [16]). In the buffer zone method, that will be presented in this paper, the solution is first obtained in the combined solid-fluid domain, and then corrected inside the solid to the desired value by imposing the boundary conditions. Similar approaches have been widely used in the literature for a variety of physical problems. Kreiss et al. [17] developed a Cartesian embedded boundary method for the second order wave equation. An explicit adaptive embedded boundary method was developed for an unsteady inviscid compressible flows in [18]. It was extended to solve a variable coefficient Poisson equation and coupled to an AMR framework in [19]. Fedkiw et al. [20] used a ghost fluid method to preserve continuity of pressure and velocity profiles at discontinuous interfaces (tracked by a level set approach) in two-phase incompressible flows. Deiterding [21] used this approach, coupled to an AMR framework, to investigate gaseous detonations.

Breugem and Boersma [22] presented a method for non-reacting cold flow simulation in a porous media using Cartesian mesh-aligned solid cubes in a three-dimensional fluid domain. An IBM variant has been proposed for conjugate heat transfer problems with moving and stationary particles, as well as constant and variable temperature particles; using RANS models in [23] and using LES/DNS models in [24]. For low-Mach number flows, Paravento et al. [25] proposed an IBM to include heat exchange between a Cartesian grid-aligned rectangular object and the non-reacting single-species fluid surrounding it. However, this method was not generalized for flows with varying (temperature and composition dependent in reacting flows) thermal conductivity. These challenges are further compounded by the presence of chemical reactions and multi-species transport equations. Henshaw and Chand [26] described an approach to incorporate conjugate-heat exchange using composite overlapping grids. The solid and the fluid domains are solved separately and the solutions were coupled at the boundary. IBM for reacting flows with fully coupled momentum-species-energy transport and conjugate heat exchange with complex immersed walls are not yet developed to the best of our knowledge.

In an effort toward bridging this gap, in this paper we present a second-order "buffer zone" IBM to incorporate flame-wall interactions and couple it with the numerical development presented in [12]. We limit the current discussion to a Cartesian-grid conforming immersed solid. Using this new method, we simultaneously tackle (a) Cartesian mesh-aligned immersed wall undergoing conjugate heat exchange with the surrounding reacting flow, (b) multiscale processes using the operator-split projection scheme, (c) detailed chemical kinetics for multi-species transport, and (d) dynamic tracking of the flame with SAMR. We describe the numerical method in Section 2. Grid convergence studies, validation and a reacting flow simulation are presented in Section 3 and the paper is summarized in Section 4.

2. Governing equations and numerical methodology

The operator-split projection method using the SAMR framework, developed for chemically reacting flows in [12] for fluid-only domains, forms the basis of our current work. In this section we briefly summarize it and then couple it with the new buffer zone method to accurately incorporate flame-wall interactions.

2.1. SAMR framework

SAMR is used to adaptively refine the computational grid in regions where the internal flame structure needs to be resolved accurately. Figure 1 shows a schematic illustration of the SAMR grid topology. A relatively coarse Cartesian mesh is laid over the entire domain and the field variables are initialized on it. The grid cells are collated into rectangular patches and finer grids, known as *children* patches (obtained by splitting each cell in half in each dimension) are recursively formed in regions of sharp gradients (based on temperature or the species of choice). A layer of ghost cells are added to each patch at all levels to allow the use of symmetric stencils for derivatives and interpolations. The adaptive nature of SAMR arises from the periodic process of identifying cells requiring refinement (followed by the addition of finer patches) and the simultaneous coarsening of regions which no longer require refinement. In the current implementation, the momentum equations are discretized and solved on a uniform mesh only, and are coupled to the solution of the species and energy conservation equations on the adaptive mesh hierarchy. For a typical premixed flame, scalar gradients are much sharper than velocity gradients. The characteristic thickness of the reaction zone of the flame (typical of the scalar length-scales) is approximately 5$\sim$10 times smaller than the characteristic thickness of the convection-diffusion zone (typical of the velocity length-scales) for a conventional hydrocarbon flame[1]. Moreover, the integration of the momentum equations is typically a small fraction ($\sim$ 10%) of the total iteration time [12]. Thus it is efficient to choose a uniform base grid capable of fully resolving the velocity field and using the SAMR hierarchy only for the scalars. This is additionally advantageous because one avoids the complex pressure Poisson solver on the SAMR grid in the projection step, which is currently much slower than its uniform grid counterpart.

A binary marker function (value 1 in the solid and value 0 in the fluid) is used as indicator for the solid cells at all the levels of refinement. The entire domain is treated as a single-material (fluid-only) domain with physical properties (heat conductivity, specific heat and density) appropriately changed in the solid region using the marker function. Layers of fictitious

---

[1] $\frac{\delta_R}{\delta_T} \approx \frac{n}{Z}$ for a premixed flame where δ_R is the reaction-diffusion zone thickness, δ_T is the convection-diffusion zone thickness, n is the overall reaction order ($\approx$ 1-3 for methane-air combustion) and Z is the Zeldovich number ($\approx$ 11 for methane-air combustion)

cells, called a buffer zone in the paper, are created within the numerical domain near the solid-fluid boundary and their values are filled such that the boundary conditions get imposed automatically when the derivative and interpolation routines are implemented. This allows the usage of symmetric stencils throughout the interior of the domain. The marker function approach allows for disjoint multiple solid objects in the computational domain; useful for practical applications such as flow simulation around an array of heat-conducting flame-holders in a combustor.

2.2. Governing equations

At the low-Mach number limit, the continuity, momentum and scalar equations are written in compact form as

$$\nabla \cdot \mathbf{v} = -\frac{1}{\rho}\frac{D\rho}{Dt} \tag{1a}$$

$$\frac{\partial \mathbf{v}}{\partial t} = -\frac{1}{\rho}\nabla p + C_U + D_U \tag{1b}$$

$$\frac{\partial T}{\partial t} = C_T + D_T + S_T \tag{1c}$$

$$\frac{\partial Y_k}{\partial t} = C_{Y_k} + D_{Y_k} + S_{Y_k} \quad k = 1, 2, \ldots, N_s \tag{1d}$$

where $\mathbf{v}$ is the velocity vector, ρ the density, T the temperature, Y_k the mass-fraction of species k, p is the hydrodynamic pressure, and N_s is the number of chemical species. The $\frac{D}{Dt}$ operator represents the material derivative, $\frac{D}{Dt} = \frac{\partial}{\partial t} + \mathbf{v} \cdot \nabla$. The system of governing equations is closed with the equation of state for an ideal gas

$$P_0 = \frac{\rho \Re T}{\overline{W}} = \rho \Re T \sum_{k=1}^{N_s} \frac{Y_k}{W_k} = \text{const} \tag{2}$$

where P_0 is the thermodynamic pressure, $\Re$ is the universal gas constant, W_k is the molecular weight of species k, and $\overline{W}$ is the molecular weight of the mixture. The thermodynamic pressure is spatially uniform in the low-Mach number limit. Further, restricting our focus to flow in an open domain, P_0 is assumed constant.

The convection and diffusion terms in (1) are given by

$$C_U = -\left(\mathbf{v} \cdot \nabla\right) \mathbf{v}, \qquad D_U = \frac{1}{\rho} \nabla \cdot \tau, \tag{3a}$$

$$C_T = -\left(\mathbf{v} \cdot \nabla\right) T, \qquad D_T = \frac{1}{\rho c_p} \nabla \cdot \left(\lambda \nabla T\right) - \left(\sum_{k=1}^{N_s} c_{p,k} Y_k \mathbf{V}_k\right) \cdot \nabla T \tag{3b}$$

$$C_{Y_k} = -\left(\mathbf{v} \cdot \nabla\right) Y_k, \quad D_{Y_k} = -\frac{1}{\rho} \nabla \left(\rho Y_k \mathbf{V}_k\right) \tag{3c}$$

and the source terms by

$$S_T = -\frac{1}{\rho c_p} \sum_{k=1}^{N_s} h_k \dot{\omega}_k, \qquad S_{Y_k} = \frac{\dot{\omega}_k}{\rho} \tag{4}$$

where τ is the stress tensor given by $\tau_{ij} = \mu \left(\frac{\partial u_i}{\partial x_j} + \frac{\partial u_j}{\partial x_i} - \frac{2}{3} \delta_{ij} \nabla \cdot \mathbf{v} \right)$, μ is the dynamic viscosity, and λ is the mixture thermal conductivity. Further,

$$\mathbf{V}_k = -\frac{D_{k,m}}{Y_k} \left(\nabla Y_k + \frac{Y_k}{\overline{W}} \nabla \overline{W} \right), \tag{5}$$

is the diffusion velocity of species k, where $D_{k,m}$ is the mixture-averaged diffusivity of species k. Finally, c_p and $c_{p,k}$ are the specific heats at constant pressure for the mixture and species k, respectively, and h_k and $\dot{\omega}_k$ are the specific enthalpy and molar production rate, respectively, of species k. The equation of state Eq. (2) is used to derive an expression for the right hand side of the continuity equation (1a)

$$\frac{DP_0}{Dt} = 0 \rightarrow \frac{1}{\rho}\frac{D\rho}{Dt} = -\frac{1}{T}\frac{DT}{Dt} - \sum_{k=1}^{N_s} \frac{\overline{W}}{W_k}\frac{DY_k}{Dt} \tag{6}$$

$$= -\frac{1}{T}\left(D_T + S_T\right) - \sum_{k=1}^{N_s} \frac{\overline{W}}{W_k}\left(D_{Y_k} + S_{Y_k}\right) \tag{7}$$

The Soret and Dufour effects are negligible for hydrocarbon combustion and are not included in the transport model. Radiation is ignored: a reasonable assumption for lean premixed flames because its total gas emittance (dominated by H_2O and CO_2) is typically extremely small. A mixture-averaged formulation is used to compute the transport properties of the gas mixture.

There is thermal contact between the immersed solid body and the surrounding fluid. The conjugate heat exchange between them is incorporated by simultaneously integrating the equations governing the reacting flow with the transient heat conduction equation inside the solid:

$$\frac{\partial T}{\partial t} = \frac{1}{\rho_s c_s}\nabla \cdot \left(\lambda_s \nabla T\right) \tag{8}$$

where ρ_s is the density, λ_s is the thermal conductivity and c_s is the heat capacity of the solid.

2.3. Numerical methodology

On each rectangular patch in the domain, a staggered mesh is used: variables are defined at the cell-centers (scalars) and the edge-centers (vectors).

The numerical integration of the system of equations is performed in three stages. First, a projection approach is adopted for the momentum equations on a fixed uniform mesh. In the second stage, we recursively implement a symmetric Strang splitting scheme in all the SAMR levels beginning with the chemical source term contribution for half the time step, followed by the contributions from the convection and diffusion terms for a full time step, and concluded by the remaining contribution from the reaction term for half the time step. The time stepping is concluded with the third stage, which repeats the projection algorithm for the momentum equations using the updated scalar fields. The sequential stages of the numerical algorithm to efficiently integrate the multiscale governing equations are described in detail in [12]. The major differences are highlighted in the summary below. The new buffer zone IBM to incorporate the flame-wall interactions is then presented in detail in Section 2.4.

Stage 1_a

The second-order Adams-Bashforth scheme is used to advance the velocity field from $\mathbf{v}^n$ to $\hat{\mathbf{v}}^{n+1}$ using convection and diffusion terms only, without the pressure gradient term. The rigid rectangular immersed body is stationary and the solid marker function is used to impose the no-slip condition on the provisional velocity field $\hat{\mathbf{v}}_s^{n+1} = 0$; subscript s denotes a solid cell.

Stage 1_b

The provisional velocity field, $\hat{\mathbf{v}}$, does not satisfy the continuity Eq. (1a). This equation is used in conjunction with Eq. (1b) to derive an equation for the hydrodynamic pressure field which is then used to correct $\hat{\mathbf{v}}$. A standard second-order finite-difference method is used to solve the variable coefficient pressure Poisson equation. The pressure stencil is appropriately adjusted near the computational domain boundaries and the immersed solid boundaries (using the binary marker function). Explicit pressure boundary conditions are not required because of the staggered grid arrangement. The pressure value in the cell-center of one of the corner cells in the outflow boundary of the domain is fixed to unity for uniqueness of the solution. The *hypre* package is used to solved the linear system resulting from the discretization on the uniform base grid of the mesh hierarchy. The iterative conjugate gradient method is used with the tolerance for the residuals typically set to 10^{-14}–10^{-17} (limits the propagation of convergence errors).

Stage 1_c

The gradient of the hydrodynamic pressure is then used to correct the provisional velocity field $\hat{\mathbf{v}}^{n+1}$ to obtain the predicted velocity at $n+1$

$$\mathbf{v}^{n+1,p} = \hat{\mathbf{v}}^{n+1} - \frac{\Delta t}{\rho^{n+1}} \nabla p, \tag{9}$$

Superscript p refers to the predicted velocity values.

Stage 2_a

The scalars (temperature and species mass fractions) are advanced over half the time step based on contributions from the source terms, S_T and S_{Y_k}.

$$\begin{aligned} T^* - T^n &= \int_{\Delta t/2} S_T dt \\ Y_k^* - Y_k^n &= \int_{\Delta t/2} S_{Y_k} dt \quad k = 1, 2, \ldots, N_s \end{aligned} \tag{10}$$

The CVODE stiff integrator package [27] is used to implicitly integrate Eqs. (10). The source terms for species and energy equations are set to zero for the solid body using the binary marker function.

Stage 2_b

A second-order, multi-stage, Runge-Kutta-Chebyshev (RKC) explicit scheme is used to advance scalars based on the contributions from convection and diffusion terms. The convection terms for species and energy equations are zero for the solid cells since the velocity field is zero. The no penetration boundary condition for species mass-fractions and the conjugate heat exchange matching conditions for temperature, discussed later, are imposed at each RKC stage.

Stage 2_c

Stage 2_c is a repeat of Stage 2_a, using the "**" scalar values as initial conditions. At the end of this stage all scalars correspond to t^{n+1}.The species mass-fraction of the diluent (N_2 for air combustion) is computed by imposing the consistency condition $\sum_k Y_k = 1$.

Time integration on the mesh hierarchy

Temperature and species mass-fractions have to be integrated on the successively refined mesh in the SAMR framework. On adjacent mesh levels, L and $L+1$ in the grid (see Fig. 1), the scalars are first advanced on the coarse level L using the RKC algorithm described above. After the advancement is completed on L, the solution on this level is used to provide boundary conditions (via coarse-to-fine prolongation) for the solution advancement on $L+1$. The grid size on the finer mesh level $L+1$ is half compared to L.

The time step is also halved for stability purposes. At the end of the two sub-steps on $L+1$ the fine-grid solution is interpolated to the coarse grid L via fine-to-coarse restriction.

Stage 3_a

The provisional velocity field values at t^{n+1} are re-evaluated based on the scalar values obtained at the end of Stage 2 and on the predicted velocity values at the end of Stage 1. Similar to the Stage 1_a, the no-slip boundary condition at the immersed boundaries is imposed using the binary marker function.

Stage 3_b

The hydrodynamic pressure field is re-computed using the provisional velocity field obtained in Stage 3_a.

Stage 3_c

This final stage in the iteration is similar to Stage 1_c. The gradient of the hydrodynamic pressure obtained at Stage 3_b is used to correct the velocity obtained at the end of Stage 3_a.

The interpolation and derivative stencils are chosen such that an overall second-order accuracy is achieved. A fourth-order accurate derivative stencil is used for all the terms in the governing equations where second-derivatives need to be computed (e.g. the diffusion terms). This is because we compute the second derivative by taking the derivative of the first derivative. A second-order accurate derivative stencil is used for all the terms in the governing equations where only a first-derivative needs to be computed (e.g. the convection terms). We use second-order stencils for the interpolations required during the multigrid prolongation and restriction. The interpolation and derivative stencils for various orders of accuracy are presented in [28]. A detailed investigation of the computational expense of each of the algorithmic components was presented in [12]. It was shown that typically Stage 2 consumes the majority of the computational time.

Boundary conditions

The domain boundary conditions are the same as described in [12]. In addition, we impose the no-slip boundary condition and the following scalar matching conditions at each cell edge at the solid-fluid boundary of the immersed object.

- Temperature matching $T|_{fluid} = T|_{solid}$
- Heat flux matching $\lambda\frac{\partial T}{\partial n}|_{fluid} = \lambda\frac{\partial T}{\partial n}|_{solid}$
- No penetration of species $\frac{\partial Y_i}{\partial n}|_{fluid} = 0$

These matching conditions are imposed using the novel buffer zone approach described in the next section.

2.4. Buffer zone method

The buffer zone approach is introduced here: the solution is first obtained in the combined solid-fluid domain, and then corrected inside the solid to the desired value by imposing the boundary conditions. Similar techniques are well developed in the literature for non-reacting flows, even for complex non-grid conforming immersed solid bodies. However a methodology similar to the one described in the following section, that solves multi-species reacting flows in the SAMR framework incorporating solid-fluid conjugate heat exchange, is still missing to the best of our knowledge.

Buffer zones, comprised of a very thin layer of fictitious valued-cells, are employed near the solid-fluid boundary inside the numerical domain. These cells are created at each sub-step of the scalar RKC integration in Stage 2 such that the boundary matching conditions are automatically imposed when the symmetric stencils are used within the solvers for computing derivatives and interpolations. This makes the numerical implementation simpler as the entire domain can then be regarded as a fluid-only domain. The no-penetration of the species is imposed by using single-sided buffer zones and the temperature and heat flux matching conditions are imposed by using dual buffer zones.

2.4.1. Single-sided buffer zones for species mass-fractions

Due to the presence of second derivatives in the diffusion terms, the right-hand-side term in Eq. (1d) at each cell center then depends on a 3×3 grid cells around it (for a two dimensional stencil). Thus, to impose the no-penetration of species condition at the fluid-solid boundary, a 3-cell deep layer of buffer zone is created inside the rectangular solid body, refer to Fig. 2a for a schematic illustration. The species mass-fractions do not physically exist inside the immersed solid object allowing us to re-use the solid cells' data structures originally defined assuming they were fluid cells. This construction does not add significantly to the iteration cost because the number of cells in the buffer zones are a very small fraction of the total number of cells in the full numerical domain.

Consider, for simplicity, a one-dimensional configuration, with the indices for the cell and edge centers as shown in Fig. 2b. The zero-gradient scalar no penetration condition, $\frac{\partial f}{\partial x} = 0$, at the face center of the solid-fluid boundary using a 4^{th} order accurate derivative stencil and 4^{th}order extrapolations for cells (-2) and (-3) gives

$$\begin{aligned} \frac{1}{24h_x}\left(f_{-2} - 27f_{-1} + 27f_0 - f_1\right) &= 0 \\ f_{-2} - 4f_{-1} + 6f_0 - 4f_1 + f_2 &= 0 \\ f_{-3} - 4f_{-2} + 6f_{-1} - 4f_0 + f_1 &= 0 \end{aligned} \tag{11}$$

leading to

$$\begin{aligned} f_{-1} &= \frac{1}{23}\left(21f_0 + 3f_1 - f_2\right) \\ f_{-2} &= \frac{1}{23}\left(-54f_0 + 104f_1 - 27f_2\right) \\ f_{-3} &= \frac{1}{23}\left(-250f_0 + 375f_1 - 102f_2\right) \end{aligned} \tag{12}$$

These expressions are used to construct the buffer zone for the species mass-fractions inside the solid. The fluid cells adjacent in the y-direction are used as 0, 1 and 2 for the y-normal edge of the solid body. Similarly the fluid cells adjacent in the x-direction are used as 0, 1 and 2 for x-normal edge.

Corner treatment

Special corner treatment is required for the 4 corners of the immersed solid because of the ambiguity in the direction to choose. The buffer zone is modified in the 3×3 cells in each corner, see Fig. 3 for a schematic illustration.

A set of 9 consistent equations with these 9 unknowns are formulated and the corner cells (marked as 1, 2, 3 ..., 9 in Fig. 3) are appropriately filled. A zero-gradient condition is imposed at the solid-fluid faces adjacent to cells 2, 3, 4 and 7. Corner point (cell 1) is a numerical singularity and does not exist in reality. Hence we approximate a zero-gradient along the diagonal of cell 1. This results in

$$\begin{aligned}\frac{1}{h_y}\left(f_5 - 27f_2 + 27f_{b0} - f_{b1}\right) &= 0\\ \frac{1}{h_y}\left(f_6 - 27f_3 + 27f_{c0} - f_{c1}\right) &= 0\\ \frac{1}{h_x}\left(f_5 - 27f_4 + 27f_{f0} - f_{f1}\right) &= 0\\ \frac{1}{h_x}\left(f_8 - 27f_7 + 27f_{g0} - f_{g1}\right) &= 0\\ \frac{1}{\sqrt{h_x^2 + h_y^2}}\left(f_5 - 27f_1 + 27f_{d0} - f_{d1}\right) &= 0\end{aligned} \tag{13}$$

where h_x and h_y are the grid spacings in the x and y directions respectively. 4$^{\text{th}}$order extrapolations along the diagonal direction are chosen for cells 5 and 9, along the x-direction for cell 8 and along the y-direction for cell 6 on the basis of proximity. This results in

$$\begin{aligned}(f_5 - 4f_1 + 6f_{d0} - 4f_{d1} + f_{d2}) &= 0\\ (f_9 - 4f_5 + 6f_1 - 4f_{d0} + f_{d1}) &= 0\\ (f_8 - 4f_7 + 6f_{g0} - 4f_{g1} + f_{g2}) &= 0\\ (f_6 - 4f_3 + 6f_{c0} - 4f_{c1} + f_{c2}) &= 0\end{aligned} \tag{14}$$

Above is a set of 9 equations and 9 unknowns (Scalar values f_1, f_2, ..., f_9) based on 21 knowns ($f_{a0}, f_{a1}, f_{a2},\ f_{b0}, f_{b1}, f_{b2},\ \ldots\ ,\ f_{g0}, f_{g1}, f_{g2}$). The explicit solution is

$$\begin{aligned}
f_1 &= \frac{1}{23}\left(21 f_{d0} + 3 f_{d1} - f_{d2}\right) \\
f_2 &= f_{b0} - \frac{1}{27} f_{b1} - \frac{2}{23} f_{d0} + \frac{104}{621} f_{d1} - \frac{1}{23} f_{d2} \\
f_3 &= \frac{1}{23}\left(21 f_{a0} + 3 f_{a1} - f_{a2}\right) \\
f_4 &= f_{f0} - \frac{1}{27} f_{f1} - \frac{2}{23} f_{d0} + \frac{104}{621} f_{d1} - \frac{1}{23} f_{d2} \\
f_5 &= \frac{1}{23}\left(-54 f_{d0} + 104 f_{d1} - 27 f_{d2}\right) \\
f_6 &= \frac{1}{23}\left(-54 f_{a0} + 104 f_{a1} - 27 f_{a2}\right) \\
f_7 &= \frac{1}{23}\left(21 f_{g0} + 3 f_{g1} - f_{g2}\right) \\
f_8 &= \frac{1}{23}\left(-54 f_{g0} + 104 f_{g1} - 27 f_{g2}\right) \\
f_9 &= \frac{1}{23}\left(-250 f_{d0} + 375 f_{d1} - 102 f_{d2}\right)
\end{aligned} \tag{15}$$

Eqs. (12) and (15) together form the stencils for the single-sided buffer zones for the species mass-fraction fields. They are constructed for each species at all the levels of the SAMR grid and at every sub-step of the multistage RKC integration of the scalar field.

We performed a simple test to check the second-order accuracy of the constructed stencils. These stencils incorporated a zero-gradient (no penetration) condition of the species mass-fractions at the solid-fluid boundary. To test for its accuracy, we first analytically manufactured a test-field with circular contours around a reference point. We then constructed the 3-cell wide single-sided buffer zone near two perpendicular lines originating from that reference point (normal to the circular contours). The manufactured test-field and the reconstructed field were then compared for order of accuracy estimation. Figure 4 shows a uniformly discretized 256 × 256 square domain. We chose the point corresponding to index (176+1/2,176+1/2) as the reference origin (x_0, y_0) and computed the analytical distance ($d = \sqrt{(x - x_0)^2 + (y - y_0)^2}$) of all the points in the numerical domain from it. The left plot in Fig. 4 shows the distance contours of the manufactured test field; which are circular around the reference point by mathematical construction. Two perpendicular line segments with the indices; (1) $i = (176 + 1/2)$ and $(176+1/2) \leq j \leq 256$ and (2) $(176+1/2) \leq i \leq 256$ and $j = (176+1/2)$ were chosen as left and bottom edges of a 80 × 80 square in the top right corner of the domain. The contours of the test field are normal to these lines. We reconstructed the test field in the 3-cell wide buffer zone marked by the region $177 \leq i, j \leq 179$ using the single-sided buffer zone stencils. The manufactured test-field and the reconstructed field were compared for the error using the ℓ_1 norm ($\ell_1 = \frac{\sum_{ij} |d_{ij} - d_{ij,a}|}{N_p}$). We repeated this by decreasing the resolution: 128×128 discretization of the domain with reference point as (88+1/2,88+1/2). The order of accuracy was computed [29] to be $\log_2 \frac{L_{1,256}}{L_{1,128}} = 2.03$. This manufactured solution test confirmed the second-order accuracy of the single-sided buffer zone stencil. Detailed overall convergence order tests using various reacting and non-reacting flows will be discussed in Section 3.

Note

3$^{\text{rd}}$ order extrapolations for cells (-2) and (-3) may be used instead of 4$^{\text{th}}$-order extrapolations to reduce numerical oscillations during a rapid transient such as an artificial initial condition of ignition during the start of a combustion simulation. We observed that this reduces the overall order of accuracy to 1. We describe the stencil for such a construction below. Similar to what was done before:

$$\begin{aligned}\frac{1}{24h_x}\left(f_{-2}-27f_{-1}+27f_0-f_1\right)&=0\\ f_{-2}-3f_{-1}+3f_0-f_1&=0\\ f_{-3}-3f_{-2}+3f_{-1}-f_0&=0\end{aligned} \tag{16}$$

leading to

$$\begin{aligned}f_{-1}&=f_0\\ f_{-2}&=f_{-1}\\ f_{-3}&=3f_1-2f_0\end{aligned} \tag{17}$$

The corresponding lower order corner point stencil is

$$\begin{aligned}
f_1 &= f_{d0} \\
f_2 &= f_{b0} - \frac{1}{27} f_{b1} + \frac{1}{27} f_{d1} \\
f_3 &= f_{a0} \\
f_4 &= f_{f0} - \frac{1}{27} f_{f1} + \frac{1}{27} f_{d1} \\
f_5 &= f_{d1} \\
f_6 &= f_{a1} \\
f_7 &= f_{g0} \\
f_8 &= f_{g1} \\
f_9 &= 3 f_{d1} - 2 f_{d0}
\end{aligned} \tag{18}$$

Although the buffer zone construction is shown for a two-dimensional immersed object, it can be easily extended to three-dimensions. The corner will then correspond to a 3 × 3 × 3 cube instead of a 3 × 3 square and an equivalent 27-point stencil can be analogously derived. The 9-point stencils derived above can be directly used for the sharp edges of the 3D immersed object.

2.4.2. Dual buffer zones for temperature

The numerical approach for buffer zones described in the previous section is valid for the species mass-fractions as they cease to exist inside the solid body. The buffer zones were constructed based on the values in the fluid. Thus, for computing derivatives and interpolations near the solid-fluid boundary, in the fluid domain, these variables are continuous and smooth.

This is not the case for the non-smooth temperature field. The temperature field has a discontinuity in its derivative (a kink) at the fluid-solid boundary in non-isothermal flows because of a large jump in the thermal conductivity: two orders of magnitude jump at an air-ceramic boundary and even higher for an air-metal boundary. Most conventional high-order accurate derivatives and interpolations stencils failed near such a boundary and reduced the overall accuracy because their derivation assumes a smooth field variable.

In this section, we formulate a dual buffer zone approach to address this issue. We construct two temperature fields in the numerical domain. One corresponds to the fluid domain solution (T^f) with a 2-cell wide buffer layer penetrating inside the solid domain, similar in concept to the single-sided buffer zone discussed above. The other complementary field corresponds to the solid domain solution (T^s) with a 2-cell wide buffer layer penetrating inside the fluid domain. Figure 5a shows a schematic of the dual buffer zone. Both temperature fields are the same at all the grid points in the numerical domain, except in the 4-cell wide layer of cells around the solid-fluid boundary. This construction, like the single-sided buffer zones, does not add significantly to the cost of each iteration because the number of cells in the buffer zones are again a small fraction of the total number of cells in the full numerical domain. The increase in the memory requirement is also minor because only one additional field needs to be stored in the computational memory along with all the primary variables (temperature, pressure, velocity-field, species mass-fractions) and other auxiliary variables during each iteration. The two temperature fields are independently smooth in their valid domain and their corresponding buffer zones. This allows the conventional derivative and interpolation stencils operating on T_s and T_f to each be of high-order accuracy.

The dual buffer cells are constructed sequentially such that the matching conditions at the fluid-solid boundary ($T^s = T^f$ and $\lambda_f \frac{\partial T^f}{\partial n} = \lambda_s \frac{\partial T^s}{\partial n}$) discussed in Section 2.3 are imposed. The buffer cells (-1) are first constructed by matching the 4$^{\text{th}}$order interpolations for temperature and and 4$^{\text{th}}$order accurate derivatives for flux matching on the boundary from both the solid and the fluid sides. This gives

$$\begin{aligned}\frac{1}{8}(3T^s_{-1} + 6T^s_0 - T^s_1) &= \frac{1}{8}(3T^f_{-1} + 6T^f_0 - T^f_1)\\ \frac{\lambda_s}{24}(-23T^s_{-1} + 21T^s_0 + 3T^s_1 - T^s_2) &= -\frac{\lambda_f}{24}(-23T^f_{-1} + 21T^f_0 + 3T^f_1 - T^f_2) \quad (19)\end{aligned}$$

where λ_s and λ_f are the thermal conductivities of the solid and the fluid cells respectively. The same matching conditions are then satisfied using a symmetric 4$^{\text{th}}$order stencil as

$$\begin{aligned}\frac{1}{16}(-T^s_{-2} + 9T^s_{-1} + 9T^s_0 - T^s_1) &= \frac{1}{16}(-T^f_{-2} + 9T^f_{-1} + 9T^f_0 - T^f_1)\\ \frac{\lambda_s}{24}(T^s_{-2} - 27T^s_{-1} + 27T^s_0 - T^s_1) &= -\frac{\lambda_f}{24}(T^f_{-2} - 27T^f_{-1} + 27T^f_0 - T^f_1) \quad (20)\end{aligned}$$

Equations (19) and (20) are sequentially solved to fill (-1) and (-2) cells. A third set of conditions is required because the second derivative of the temperature (computed for the thermal diffusion) needs a 3$^{\text{rd}}$buffer cell for computation. We choose a 4$^{\text{th}}$-order extrapolation condition on the heat flux $F_i = \lambda_i \frac{\partial T_i}{\partial n}$. The heat fluxes are computed on the face centers of the staggered grid. The imposed extrapolation is

$$
\begin{aligned}
F^f_{-3/2} &= 4F^f_{-1/2} - 6F^f_{1/2} + 4F^f_{3/2} - F^f_{5/2} \\
F^s_{-3/2} &= 4F^s_{-1/2} - 6F^s_{1/2} + 4F^s_{3/2} - F^s_{5/2}
\end{aligned}
\tag{21}
$$

If the thermal conductivity is constant in both the fluid and the solid domains, Eqs. (21) gets simplified in terms of a temperature value at the third buffer cell (-3) using 4th order accurate derivative stencils as

$$
\begin{aligned}
T^f_{-3} &= 31T^f_{-2} - 141T^f_{-1} + 275T^f_0 - 275T^f_1 + 141T^f_2 - 31T^f_3 + T^f_4 \\
T^s_{-3} &= 31T^s_{-2} - 141T^s_{-1} + 275T^s_0 - 275T^s_1 + 141T^s_2 - 31T^s_3 + T^s_4
\end{aligned}
\tag{22}
$$

However, the thermal conductivity varies for a reacting flow and using Eq. (22) exhibited numerical instabilities. We use Eqs. (21) in our implementation.

Like the single-sided counterpart, the dual buffer zones are constructed at all the levels of the SAMR grid and before the beginning of each stage in the multistage RKC scheme (Stage 2_b in the algorithm). Thereby, the conjugate heat exchange condition is enforced at the beginning of each sub-stage. In a multi-species transport simulation, the iteration time-step size is already small enough to ensure that errors are small in between two stages of the multistage RKC, when the conjugate heat exchange condition is not explicitly enforced. The dual buffer zones are required only for the construction of the thermal diffusion term in the energy equation. We thus compute this term sequentially by sweeping first in the x-direction and then in the y-direction. More specifically, the thermal diffusion due to the y-gradients in temperature is first ignored and the dual buffer zones are formed in the x-direction and the diffusion term is computed. The thermal diffusion due to the x-gradients in temperature is then ignored and the dual buffer zones are formed in the y-direction and the diffusion term is computed. These two terms are then added to get the total thermal diffusion in each cell for the two-dimensional domain. This allows us to avoid the sharp corner treatment as was necessary for the species mass-fraction fields[2].

A conceptually similar Matched Interface and Boundary method was presented by Zhou et al. [30]. They outlined a generalized method to obtain high-order accurate solution of elliptic equations with discontinuous coefficients and singular sources on Cartesian grids. They successfully demonstrated it using non-reacting test cases with non-grid conforming immersed boundaries. However, a method for a more complex problem such as multi-species reacting flows was not formulated. A second-order buffer zone IBM coupled with an operator-split projection algorithm and SAMR framework for multi-species reacting flows is unique in our method. Complex immersed boundaries-SAMR coupling (irregular geometries with boundary cutting through the grid cells) is a far more challenging task and a natural extension to our current work.

---

[2] 2nd derivatives of the species mass-fractions need to be computed multiple times per iteration making the alternate direction sweeping technique used for the dual buffer zone cumbersome for implementation in our numerical method

3. Results and discussions

In this section, we validate the overall construction and demonstrate its second-order temporal and spatial convergence using various test cases. We also demonstrate the capability of our numerical method using a two-dimensional reacting flow simulation of a premixed methane/air flame stabilized on a channel-confined bluff-body.

3.1. Impulsively started thin vertical plate in a non-reacting isothermal cross-flow: validation and temporal convergence

The flow past a thin flat plate normal to the free stream is a classic example of bluff-body flows. We use this test case to validate the no-slip implementation and the pressure solver in the presence of the immersed solid in the momentum integration stages, which is solved only on a uniform grid as noted before. We consider a fixed vertical plate of height d in a cross-flow where the undisturbed velocity far away from the plate is U. This configuration has been extensively used for benchmarking in the literature; experiments of Taneda and Honji [31] and Dennis et al. [32], finite element simulations of Yoshida and Nomura [33], Laval and Quartapelle [34] and Tamaddon-Jahromi et al. [35], vortex method simulation of Koumoutsakos and Shiels [36]. As the plate is impulsively started, a recirculation zone starts to form on the downstream face of the thin vertical plate and it starts to grow with time. Figure 6 shows a comparison of the location of this growing symmetric recirculation during its early development. The recirculation zone size is defined as the distance of the downstream stagnation point from the downstream edge of the plate. An inflow $\mathrm{Re_d} = 126$ based on d was chosen in the simulation. The thickness of the plate was used as $0.15d$, where $d = 5$mm. 320×128 grid points were used with the domain size of $20d\times12.5d$. Symmetry conditions were used at the boundaries parallel to the flow direction. Figure 6 shows an excellent agreement with the transient data documented in the literature; here the lengths and velocities are nondimensionalized by d and U respectively. For a better visualization, a representative streamline pattern and vorticity at an intermediate time instant is shown in the insert of Fig. 6. The scatter in the literature data increases with the non-dimensional t^* due to the increasing influence of the boundaries parallel to the flow depending on the experimental conditions and the numerical approximation.

We further used the above uniform grid isothermal case to verify that an overall second-order temporal accuracy is achieved. Projection methods for incompressible flows have been reported to be potentially first-order accurate in time in the presence of a no-slip wall due to the ambiguity in the boundary conditions to be used for the intermediate velocity field before the pressure Poisson correction [37, 38]. Weinan and Liu [38] reviewed the different boundary conditions proposed for the intermediate velocity field to achieve an overall second-order temporal accuracy. We did not use any such corrections but still observed that the second-order temporal accuracy was maintained. As discussed in the numerical method, we impose a no-slip wall boundary condition for the intermediate velocity field. The unsteady test case discussed above was simulated for $t^* = 1$ (corresponding to time when the recirculation zone length is almost equal to the plate height d) using three different time-steps: coarse $dt^* = \frac{t^*}{1000}$, medium $dt^* = \frac{t^*}{2000}$ and fine $dt^* = \frac{t^*}{4000}$. The spatial grid resolution was the same in all the three simulations and the

	O_{ℓ_1}	$err_{1,c-m}$	$err_{1,m-f}$
u	1.97	7.062e-9	1.808e-9
v	2.00	1.171e-8	2.919e-9

Table 1: Temporal convergence orders for the uniform grid simulation of an impulsively started thin vertical plate in a cross flow.

ℓ_1 norms were used to compute the errors.

$$\ell_1 = \frac{\sum_{i,j} \mid (\phi_{i,j} - \phi_{i,j,ref}) \mid}{N_p} \tag{23}$$

where N_p is the number of grid points. The grid convergence order was then estimated as [29]

$$O_{\ell_1} = \log_2 \frac{err_{1,c-m}}{err_{1,m-f}} \tag{24}$$

where err denotes the ℓ_1 error and subscripts $c-m$ and $m-f$ denote the coarse and medium temporal errors when compared to the medium and fine time-step simulations respectively. The temporal convergence orders are shown in Table 1. The overall second-order temporal accuracy is verified.

3.2. Unsteady non-reacting isothermal flow: validation

We present another unsteady cold flow validation of the momentum transport using a uniform 320 × 128 grid simulation. A fully developed parabolic inlet profile for the streamwise velocity was assumed. Figure 7 shows the instantaneous vorticity contours of an unsteady channel-confined cold flow around a square cylinder at $\mathrm{Re_d} = 100$ for a blockage ratio $d/H = 0.2$, where H is the y-direction width of the computational domain. The vorticity was non-dimensionalized by the global maximum value. The cold flow was observed to be unsteady at these conditions. For this flow, the value of the Strouhal number $\mathrm{S_d} = \frac{fd}{U}$ reported by Suzuki et al. [39] was 0.222 (on a stretched 207 × 54 grid points two-dimensional simulation); f is the frequency of vortex shedding. We calculated this to be $\mathrm{S_d} = 0.232$. Figure 7 also shows that the strong vorticity near the upper and lower channel walls, associated with localized moving recirculation zones, is captured similar to observations in [40].

3.3. Steady-state conjugate heat exchange between air and a ceramic solid object: validation and spatial convergence

We present here a simple test case to validate the dual buffer zone method. We tested the accuracy of the conjugate heat exchange between stationary air having a temperature dependent thermal conductivity and a ceramic solid object of a constant thermal conductivity of $\lambda_s = 1.5$W/mK (approximately 50 times larger than air). Only the energy equation was integrated; the momentum projection and chemical source terms were decoupled from the governing equations. The number of RKC steps for Stage 2b of the numerical algorithm was fixed to $M = 8$. Symmetry conditions were imposed at y_{min} and y_{max} boundaries. Dirichlet boundary conditions for temperature were used: 300K at x_{min} and 600K at x_{max} boundaries. The steady-state solution on a 64 × 64 uniform grid was obtained, shown in the contour plot in Fig. 8. x and y were non-dimensionalized by the height of the heat-conducting solid object, d (white square in Fig. 8). In the absence of any immersed solid, the temperature would increase "almost" linearly from x_{min} to x_{max}; a small nonlinearity resulting from the temperature dependence of the thermal conductivity of air. This is seen near the y_{min} and y_{max} boundaries in Fig. 8(top), where the influence of the immersed solid is small. The temperature field is non-smooth at the edges of the solid body due to the large change in the thermal conductivity. For a dual buffer zone implementation, that accurately resolves the kink in T during the conjugate heat exchange, the change in the slope of T must be equal to the thermal conductivity ratio. Fig. 8(bottom) shows the temperature kink at the left and the right edge of the immersed solid. We verified this jump at each edge to be equal to the thermal conductivity ratio of the solid and the air at the corresponding temperature; thereby validating the dual buffer zone construction.

We further verified the spatially second-order convergence of our method using the above test-case using three simulations. The steady-state simulations were obtained on fine (64×64 base grid + 2 levels of refinement equivalent to a grid size of 256×256), medium (64×64 base grid + 1 level of refinement equivalent to a grid size of 128×128) and coarse (a unilevel 64×64) grids. The temperature solution fields for the three grids at the coarsest (base) grid level were compared. Again, the ℓ_1 norm (Eq. 23) was used to compute errors. The convergence order of 2.19 was obtained showing that the non-smooth temperature profile was resolved with a second-order accuracy using the dual buffer zone method.

3.4. Convection-diffusion test: spatial convergence

The momentum and scalar transport equations were coupled with the SAMR framework in the simulations discussed in the remaining sections. Both single-sided and dual buffer zones were thus constructed simultaneously.

Figure 9 shows a 2-level flow simulation of a Gaussian field of temperature and species mass-fraction around an immersed rectangular solid. The black rectangles mark the refined patches in the domain. The outer rectangle is the level 1 patch refined by factor of 2 from the base grid and the inner rectangle is the level 2 patch refined further by a factor of 2 from the level 1 grid. The flow direction is from left to right. The flow was composed of a non-reacting mixture of 2 species (CH_4 and N_2). The chemical source terms were switched off during this test case, thereby considering a non-isothermal but non-reacting multi-species simulation. An initial condition of an upstream Gaussian scalar field of T, Y_{CH_4} and Y_{N_2} was specified (note that $\sum_k Y_k = 1$ and thus $Y_{N_2} = 1 - Y_{CH_4}$) such as

$$\phi(x/d, y/d) = \phi_0 \exp(-\frac{(x/d - x_0)^2 (y/d - y_0)^2}{\delta^2}) \tag{25}$$

where $d = 2.4$ mm is the height of the solid body in the y-direction and non-dimensional $\delta = 0.4$, $x_0 = 1.0$ and $y_0 = 1.6$. The mean inlet flow velocity was fixed at $U = 0.3$ m/s which was equivalent to an inflow $\mathrm{Re}_d = 45$ based on d. A small time step $dt = 1 \times 10^{-5}$sec was chosen. This corresponds to convective and diffusive CFL numbers of $udt/dx = 0.05$ and $\nu dt/dx^2 = 0.05$ respectively; on the base coarse grid. The number of RKC steps for Stage $2b$ of the numerical algorithm was fixed to $M = 8$. Symmetry conditions were imposed at y_{min} and y_{max} boundaries. The thermal properties of the solid body (corresponding to steel) were $\lambda_s = 12$W/mK, $\rho_s = 8000$kg/m^3 and $c_s = 503$J/kgK. The simulation was performed for 10 ms on fine (256×128 base grid + 2 levels of refinement equivalent to a grid size of 1024×512), medium (256×128 base grid + 1 level of refinement equivalent to a grid size of 512×256) and coarse (a unilevel 256×128) grids. The flow is from left to right. The scalar solution field for the three grids at the coarsest (base) grid level were compared. The ℓ_1 norm (Eq. 23) was used to compute errors.

	O_{ℓ_1}	$err_{1,c-m}$	$err_{1,m-f}$
T	1.96	1.3667-2	3.505e-3
Y_{CH_4}	1.84	2.7467-5	7.665e-6
Y_{N_2}	1.84	2.747e-5	7.665e-6

Table 2: Spatial convergence orders for the convection-diffusion SAMR simulations.

The grid convergence order was estimated similar to the previous section; its values are shown in Table 2. The errors were computed only in the refined region in the SAMR simulations. A Gaussian field of only Y_{CH_4} and Y_{N_2} for an isothermal flow; and a Gaussian field of only T were also independently tested for convergence using the same flow conditions and convergence orders of 1.85 and 1.96 were respectively obtained.

Figure 10 shows a visualization of the single-sided buffer zone for the species mass-fraction of Y_{CH_4} corresponding to the lower right contour plot shown in Fig. 9. The contours inside the zoomed top figure visually show the fictitious values inside the single-sided species buffer zone and the zero-gradient condition at the fluid-solid boundary. It must be noted that for a refined patch, the penetration of buffer zone inside the solid is smaller since the 3-cell zone covers less area on a finer patch when compared to a coarser patch.

3.5. Reacting flow: spatial convergence

We now demonstrate the overall second-order convergence of our buffer zone method using fully-coupled reacting flow simulations.

3.5.1. Premixed flame using a single-step chemical kinetics model

Figure 11 shows the fuel (methane) contours of a premixed flame interacting with a bluff-body at the downstream end. A time-step of $dt = 1\times10^{-6}$sec, corresponding to convective and diffusive CFL numbers of 0.005, was chosen. The reactants are flowing from left to right. A global single-step chemical mechanism for methane-air combustion was chosen as

$$CH_4 + O_2 + 3.76N_2 \rightarrow CO_2 + 2H_2O + 3.76N_2 \tag{26}$$

The overall reaction rate expression for the single-step chemistry is given by

$$k_f = AT^n \exp(\frac{-E_a}{RT})[CH_4]^a[O_2]^b \tag{27}$$

where the Arrhenius constant $A = 9.0 \times 10^{23}$ cm^3/mol/sec, activation energy $E_a = 55000$ cal/moles, $a = b = 1$ were used. These values are representative of hydrocarbon combustion for a methane-air mixture [41].

The same thermal properties for the solid material, inflow $\mathrm{Re}_d = 45$ and the domain boundary conditions as used in the previous section were used for this investigation. The laminar flame speed for a stoichiometric premixed methane air flame is approximately 40 cm/s. The average streamwise velocity of 30 cm/s was chosen at the inflow, thereby resulting in an overall flame motion towards the incoming reactants in the Eulerian frame. A planar premixed flame solution using Chemkin was initialized with the flame downstream of the solid block. The solution was evolved on a coarse grid with no adaptive meshes (256×128) to a time when there was a reasonable interaction with the flame and the wall (Fig. 11 top). This solution was then used

	O_{ℓ_1}	$err_{1,c-m}$	$err_{1,m-f}$
T	2.06	2.685e+0	6.452e-1
Y_{CH_4}	2.07	6.747e-5	1.603e-5
Y_{O_2}	2.12	2.744e-4	6.330e-5
Y_{CO_2}	2.12	2.312e-4	5.295e-5
Y_{H_2O}	2.05	1.734e-4	4.196e-5
Y_{N_2}	2.00	7.598e-6	1.895e-6

Table 3: Spatial convergence orders for the premixed flame SAMR simulations using a global single-step chemical kinetics model.

as an initial condition for 3 simulations: fine (256×128 base grid + 2 levels of refinement equivalent to a grid size of 1024×512), medium (256×128 base grid + 1 level of refinement equivalent to a grid size of 512×256) and coarse (a unilevel 256×128) grids. The simulations were performed for 1ms allowing the flame to travel by approximately four reaction zone thickness length in the domain. The ℓ_1 norms for the scalars were used to estimate convergence order shown in Table 3. An overall second-order convergence was computed for all the scalar fields demonstrating the accuracy of our single-sided and dual buffer zone method in a fully coupled reacting flow simulation.

3.5.2. Premixed Flame using a detailed chemical kinetics model

We repeated the above discussed convergence test using a detailed chemical kinetics model. A 16 species 46 reactions C1 chemical kinetics described by Smooke et al. [42] was used for the simulations using similar flow conditions and domain configuration as described in the previous section. Again a simulation for a total of 1ms was performed for this test, corresponding to flame motion equivalent to approximately four reaction zone thickness. The iteration time-step was however reduced to $dt = 5 \times 10^{-7}$sec unlike the

$dt = 1 \times 10^{-6}$sec used in the single-step test. The methane contours of the premixed flame interacting with the solid at its downstream end were visually similar to the contours shown in Fig. 11. The convergence orders using the ℓ_1 norms of the major and minor species and temperature field are shown in Table 4. The overall second-order accuracy of our buffer zone method using a fully coupled reacting flow simulation, in the presence of rapidly reacting radicals, is also confirmed[3].

The SAMR simulation with 2 levels of refinement on a 256×128 base grid was observed to be 3.5× faster than the equivalent setup (same finest mesh resolution) of a unilevel 1024×512 grid. The data size of the simulation in terms of disk-space for the former was 4× smaller compared to the latter. This is indicative of the large performance gain that can be achieved for reacting flow simulations using a coupled immersed boundary-SAMR approach.

3.6. Premixed flame stabilized on a rectangular bluff-body in a confined channel

In this section, we demonstrate a practical application of our numerical method using a bluff-body stabilized premixed flame simulation. The multistep C1 skeletal mechanism was again used for defining the chemical kinetics mechanism. The reacting flow simulation around the confined rectangular cylinder is shown in Fig. 12 at $\mathrm{Re_d} = 1000$ for a blockage ratio $d/H = 0.2$. The equivalence ratio of the methane/air reactants at inflow was chosen to be $\phi = 0.7$. The flow separated at the leading edge of the flame-holder, similar to

---

[3] Additional convergence studies using the same detailed chemical kinetics model for fluid-only domains are shown in [12]

	O_{ℓ_1}	$err_{1,c-m}$	$err_{1,m-f}$
T	2.03	1.442e+0	3.526e-1
Y_{CH_4}	2.07	6.026e-5	1.433e-5
Y_{O_2}	2.07	1.952e-4	4.653e-4
Y_{CO_2}	2.06	9.373e-5	2.255e-5
Y_{H_2O}	2.04	1.104e-4	2.691e-5
Y_{CO}	2.03	7.426e-5	1.822e-5
Y_H	1.97	4.009e-7	1.026e-7
Y_{OH}	1.95	4.596e-6	1.193e-6
Y_{CH_3}	2.07	4.648e-6	1.105e-6
Y_{HCO}	1.93	1.163e-7	3.060e-8

Table 4: Spatial convergence orders for the premixed flame SAMR simulations using a detailed chemical kinetics model: C1 model described by Smooke et al. [42].

the corresponding non-reacting flow behavior on bluff-bodies [40]. The temperature contours show the conjugate heat exchange between the rectangular cylinder and the flow. The fine level patches, overlaid on the contours, show the adaptive flame tracking by the SAMR framework. The flame stabilized in the shear layer separating from the bluff-body. No artificial anchoring condition was imposed in this simulation, allowing the flame to naturally anchor near the bluff-body. This is essential to mechanistically understand the flame-stabilization physics, which is currently underway. Contours of the primary species Y_{CH_4} and the intermediate species Y_{OH} are also shown in Fig. 12. The streamlines are overlaid on the Y_{OH} contours. A recirculation zone was formed by the products of combustion behind the bluff-body. This zone plays a critical role in the flame blow-off mechanism in such configurations; detailed investigations are underway. The corresponding non-reacting isothermal flow at this $\mathrm{Re_d}$ was unsteady; associated with vortex shedding in the von Karman regime.

Temperature profile along a spanwise direction ($x/d = 2.5$) is shown in Fig. 13. The temperature field was non-smooth at the solid-fluid boundaries ($y/d = 2$ and $y/d = 3$) because of the large jump in thermal conductivity. The dual buffer zone method for the temperature ensures that this kink is well resolved and the conjugate heat exchange between the reacting flow and the flame-holder is accurately captured, as was demonstrated to be overall second-order accurate in Section 3.3. The bottom insert in Fig. 13 shows the coarse and overlaid fine mesh in a part of the computational domain. The block-structured arrangement is visible.

Additional Comments

Although currently restricted to Cartesian geometries only, our method is a step towards developing a complex immersed boundary formulation for multi-species reacting flows. Our code also has the capability of treating arbitrary geometries in the domain using stair-stepped geometries, however its accuracy is currently limited to first-order [43]. In that, we constructed a single-cell deep buffer zone for the species using a finite-volume type net-zero gradient approach. High-order complex geometry immersed boundary method (solid walls not aligned with the grid) requires accurate construction of the corresponding buffer zones and an interpolation-based implementation of the no-slip boundary condition. This is challenging and a natural extension of the current work. The modularity of our code, developed using the Common Component Architecture (CCA) framework [44], will allow the numerical machinery to be directly connected to such a complex immersed boundary formulation.

The binary marker function approach also provides an important advantage to deal with moving bodies, e.g. coal or biomass particles in combustors. In such cases tracking the moving boundary is not only expensive, but also complicated in terms of data structure implementation due to the search operations involved. Currently, to the best of our knowledge, second-order fully resolved numerical simulations with flow, thermal and chemical effects using a coupled SAMR-IBM is unavailable for moving bodies and research in this direction is also currently underway.

4. Conclusions

We introduced a spatio-temporal second-order accurate numerical method for a low-Mach number chemically reacting flow simulation near Cartesian grid-conforming immersed walls. We presented a novel buffer zone method to impose the solid-fluid boundary matching conditions eliminating the need to use one-directional stencils near the heat-conducting walls. These buffer zones coupled with a block-structured adaptively refined mesh and an operator-split projection algorithm provide a fast and efficient tool to investigate flame-wall interactions by resolving all the scales of the problem. The numerical method treats the entire domain as if it were completely fluid, allowing us to efficiently use the modular code developed using the CCA framework for fluid-only domains [12, 44]. The solid cells are tracked using a binary marker function allowing prescribing multiple solid bodies in the simulation.

We described a single-sided buffer zone construction to capture the species mass-fractions discontinuity and presented the associated stencils. The buffer zones are formed inside the solid using the zero-gradient conditions and high order extrapolations. The stencils were tested for the second-order of accuracy using a manufactured solution test. A dual buffer zone construction to capture the temperature gradient discontinuity was also introduced. A sequential construction of the buffer cells in the solid and fluid is done by imposing the boundary matching conditions maintaining an overall second-order accuracy. The buffer zones are constructed at all the levels of the SAMR grid and before each stage of the multistage RKC integration of the scalar transport. The overall second-order convergence of our buffer zone method was demonstrated using various non-reacting and reacting SAMR simulations. Validation of the code using benchmark cases from the literature was also shown. To demonstrate a practical application of our numerical method, a fully coupled reacting flow simulation with a methane-air premixed flame stabilized on a confined bluff-body, using a detailed chemical kinetics mechanism, was presented.

The accurate treatment of the flame-wall interactions through the conjugate heat exchange between the reacting flow and the nearby wall allows the flame to naturally anchor; thereby not requiring any artificial anchoring conditions often used in existing numerical investigations. Flame stabilization, extinction and blow-off mechanisms are classical multiphysics problems that we are currently investigating using this method. Other potential applications are to develop near wall sub-scale models for LES and RANS approaches for turbulent combustion.

Acknowledgments

This work was supported by King Abdullah University of Science and Technology (KAUST) award number KUS-11-010-01. This work was also supported by the US Department of Energy (DOE), Office of Basic Energy Sciences (BES) Division of Chemical Sciences, Geosciences, and Biosciences. Sandia National Laboratories is a multi-program laboratory managed and operated by Sandia Corporation, a wholly owned subsidiary of Lockheed Martin Corporation, for the U.S. Department of Energy's National Nuclear Security Administration under contract DE-AC04-94-AL85000.

References

[1] E. R. Hawkes, J. H. Chen, Direct numerical simulation of hydrogen-enriched lean premixed methane–air flames, Combustion and Flame 138 (2004) 242–258.

[2] A. Gruber, R. Sankaran, E. Hawkes, J. Chen, Turbulent flame-wall interaction: A direct numerical simulation study, Journal of Fluid Mechanics 658 (2010) 5–32.

[3] H. Najm, O. Knio, Modeling low mach number reacting flow with detailed chemistry and transport, Journal of Scientific Computing 25 (2005) 263–287.

[4] M. Day, J. Bell, Numerical simulation of laminar reacting flows with complex chemistry, Combustion Theory and Modelling 4 (2000) 535–556.

[5] K. S. Kedia, A. F. Ghoniem, Mechanism of stabilization and blowoff of a premixed flame downstream of a heat-conducting perforated plate, Combustion and Flame 159 (2012) 1055–1069.

[6] K. S. Kedia, H. M. Altay, A. F. Ghoniem, Impact of flame-wall interaction on flame dynamics and transfer function characteristics, Proceedings of the Combustion Institute 33 (2011) 1113–1120.

[7] O. M. Knio, H. N. Najm, P. S. Wyckoff, A semi-implicit numerical scheme for reacting flow, II. stiff, operator-split formulation, Journal of Computational Physics 154 (1999) 428–467.

[8] M. J. Berger, J. Oliger, Adaptive mesh refinement for hyperbolic partial differential equations, Journal of computational Physics 53 (1984) 484–512.

[9] M. Berger, P. Colella, Local adaptive mesh refinement for shock hydrodynamics, Journal of computational Physics 82 (1989) 64–84.

[10] J. Bell, M. Day, J. Grcar, M. Lijewski, J. Driscoll, S. Filatyev, Numerical simulation of a laboratory-scale turbulent slot flame, Proceedings of the Combustion Institute 31 (2007) 1299–1307.

[11] J. Bell, M. Day, M. Lijewski, Simulation of nitrogen emissions in a premixed hydrogen flame stabilized on a low swirl burner, Proceedings of the Combustion Institute 34 (2012) 1173–1182.

[12] C. Safta, J. Ray, H. N. Najm, A high-order low-mach number amr construction for chemically reacting flows, Journal of Computational Physics 229 (2010) 9299–9322.

[13] F. Duchaine, F. Boudy, D. Durox, T. Poinsot, Sensitivity analysis of transfer functions of laminar flames, Combustion and Flame 158 (2011) 2384–2394.

[14] C. S. Peskin, Numerical analysis of blood flow in the heart, Journal of Computational Physics 25 (1977) 220–252.

[15] R. Mittal, G. Iaccarino, Immersed boundary methods, Annual Review of Fluid Mechanics 37 (2005) 239–261.

[16] E. A. Fadlun, R. Verzicco, P. Orlandi, J. Mohd-Yusof, Combined immersed-boundary finite-difference methods for three-dimensional complex flow simulations, Journal of Computational Physics 161 (2000) 35–60.

[17] H.-O. Kreiss, N. A. Petersson, J. Yström, Difference approximations for the second order wave equation, SIAM Journal on Numerical Analysis 40 (2002) 1940–1967.

[18] R. B. Pember, J. B. Bell, P. Colella, W. Y. Curtchfield, M. L. Welcome, An adaptive cartesian grid method for unsteady compressible flow in irregular regions, Journal of computational Physics 120 (1995) 278–304.

[19] H. Johansen, P. Colella, A cartesian grid embedded boundary method for poisson's equation on irregular domains, Journal of Computational Physics 147 (1998) 60–85.

[20] R. P. Fedkiw, T. Aslam, B. Merriman, S. Osher, A non-oscillatory eulerian approach to interfaces in multimaterial flows (the ghost fluid method), Journal of Computational Physics 152 (1999) 457–492.

[21] R. Deiterding, Detonation structure simulation with amroc, in: High Performance Computing and Communications, Springer, 2005, pp. 916–927.

[22] W. P. Breugem, B. J. Boersma, Direct numerical simulations of turbulent flow over a permeable wall using a direct and a continuum approach, Physics of Fluids 17 (2005) 025103.

[23] G. Iaccarino, S. Moreau, Natural and forced conjugate heat transfer in complex geometries on cartesian adapted grids, Transactions of the ASME 128 (2006) 838–846.

[24] S. Kang, G. Iaccarino, F. Ham, Dns of buoyancy-dominated turbulent flows on a bluff body using the immersed boundary method, Journal of Computational Physics 228 (2009) 3189–3208.

[25] F. Paravento, M. J. Pourquie, B. J. Boersma, An immersed boundary method for complex flow and heat transfer, Flow, Turb. Combustion 80 (2008) 187–206.

[26] W. D. Henshaw, K. K. Chand, A composite grid solver for conjugate heat transfer in fluid–structure systems, Journal of Computational Physics 228 (2009) 3708–3741.

[27] P. N. Brown, G. D. Byrne, A. C. Hindmarsh, Vode: a variable-coefficient ode solver, SIAM Journal of Scientific Computing 10 (1989) 1039–1051.

[28] J. Ray, C. A. Kennedy, S. Lefantzi, H. N. Najm, Using high-order methods on adaptively refined block-structured meshes: derivatives, interpo-

lations, and filters, SIAM Journal on Scientific Computing 29 (2007) 139–181.

[29] P. J. Roache, Verification of codes and calculations, AIAA journal 36 (1998) 696–702.

[30] Y. C. Zhou, S. Zhao, M. Feig, G. W. Wei, High order matched interface and boundary method for elliptic equations with discontinuous coefficients and singular sources, Journal of Computational Physics 213 (2006) 1–30.

[31] S. Taneda, H. Honji, Unsteady flow past a flat plate normal to the direction of motion, Journal of Physical Society of Japan 30 (1971) 262.

[32] S. Dennis, W. Qiang, M. Coutanceau, J. Launay, Viscous flow normal to a flat plate at moderate Reynolds numbers, Journal of Fluid Mechanics 248 (1993) 605–605.

[33] Y. Yoshida, T. Nomura, A transient solution method for the finite element incompressible Navier-Stokes equations, International Journal for Numerical Methods in Fluids 5 (1985) 873–890.

[34] H. Laval, L. Quartapelle, A fractional-step Taylor–Galerkin method for unsteady incompressible flows, International Journal for Numerical Methods in Fluids 11 (1990) 501–513.

[35] H. Tamaddon-Jahromi, P. Townsend, M. Webster, Unsteady viscous flow past a flat plate orthogonal to the flow, Computers and fluids 23 (1994) 433–446.

[36] P. Koumoutsakos, D. Shiels, Simulations of the viscous flow normal to an impulsively started and uniformly accelerated flat plate, Journal of Fluid Mechanics 328 (1996) 177–227.

[37] J. Kim, P. Moin, Application of a fractional-step method to incompressible Navier-Stokes equations, Journal of computational physics 59 (1985) 308–323.

[38] E. Weinan, J.-G. Liu, Projection method. I: Convergence and numerical boundary layers, SIAM journal on numerical analysis 32 (1995) 1017–1057.

[39] H. Suzuki, Y. Inoue, T. Nishimura, K. Fukutani, K. Suzuki, Unsteady flow in a channel obstructed by a square rod (crisscross motion of vortex), International journal of heat and fluid flow 14 (1993) 2–9.

[40] F. Davis, F. Moore, P. Purtell, A numerical-experimental study of confined flow around rectangular cylinders, Physics of Fluids 27 (1984) 1.

[41] C. K. Westbrook, F. L. Dryer, Simplified reaction mechanisms for the oxidation of hydrocarbon fuels in flames, Combustion Science and Technology 27 (1981) 31–43.

[42] M. Smooke, I. Puri, K. Seshadri, A comparison between numerical calculations and experimental measurements of the structure of a counterflow diffusion flame burning diluted methane in diluted air, in: Symposium (International) on Combustion, volume 21, Elsevier, 1988, pp. 1783–1792.

[43] K. S. Kedia, Development of a multi-scale projection method with immersed boundaries for chemically reactive flows and its application to examine flame stabilization and blow-off mechanisms, Ph.D. thesis, Massachusetts Institute of Technology, 2013.

[44] J. Ray, R. Armstrong, C. Safta, B. Debusschere, B. A. Allan, H. Najm, Computational frameworks for advanced combustion simulations, in: Turbulent Combustion Modeling, Springer, 2011, pp. 409–437.

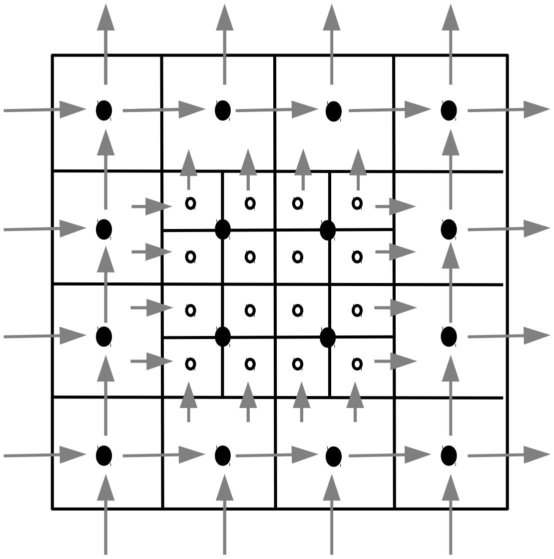

Figure 1: Schematic cell topology of a SAMR grid at two consecutive levels; filled circles are cell centers of a coarse grid level $L = 0$ and open circles are cell centers of a fine grid level $L = 1$. Velocity components are computed at the coarse grid face centers marked by large arrows and interpolated to the fine grid face centers marked by small arrows.

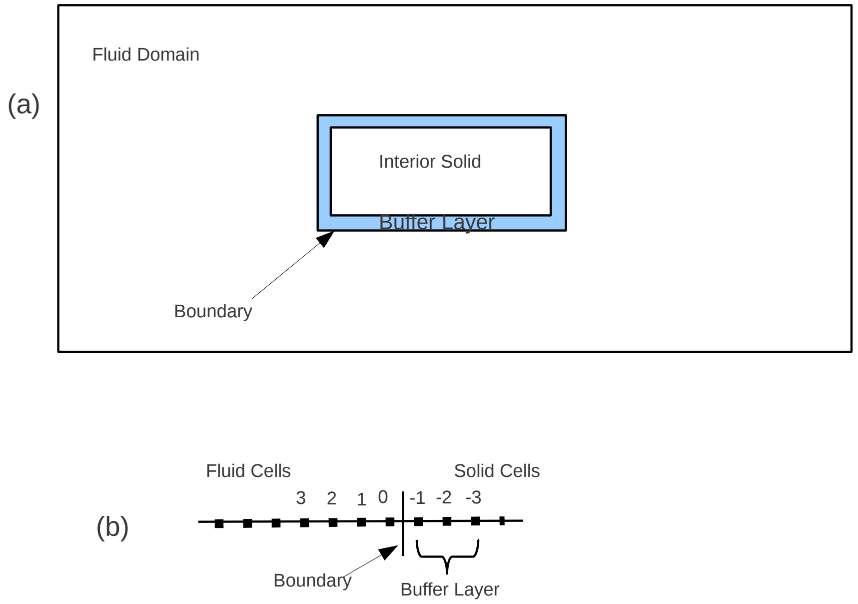

Figure 2: (a) Schematic of a Cartesian solid body inside a fluid domain; the shaded region is a 3-cell wide single-sided buffer zone (b) Cell-center indices for a one-dimensional grid marking the single-sided buffer zone.

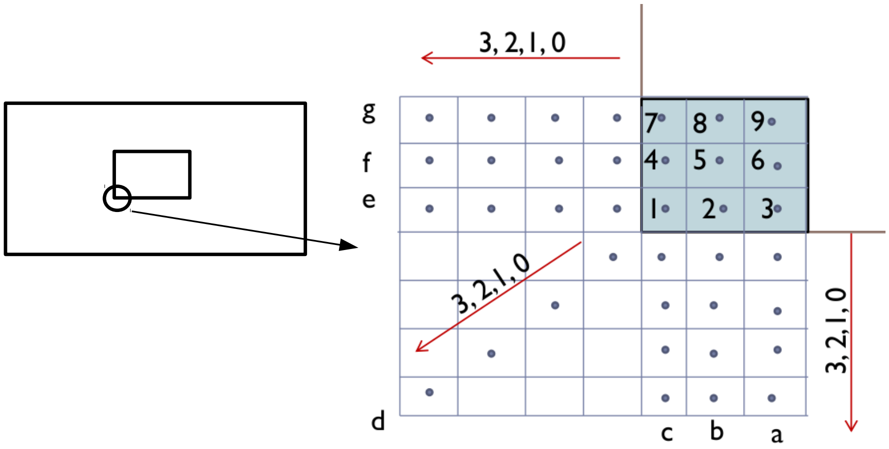

Figure 3: (left) Schematic of a Cartesian corner region inside the domain (right) Indices for the special corner treatment for the buffer zones; shaded region is the zoomed-in meshed corner inside the solid body.

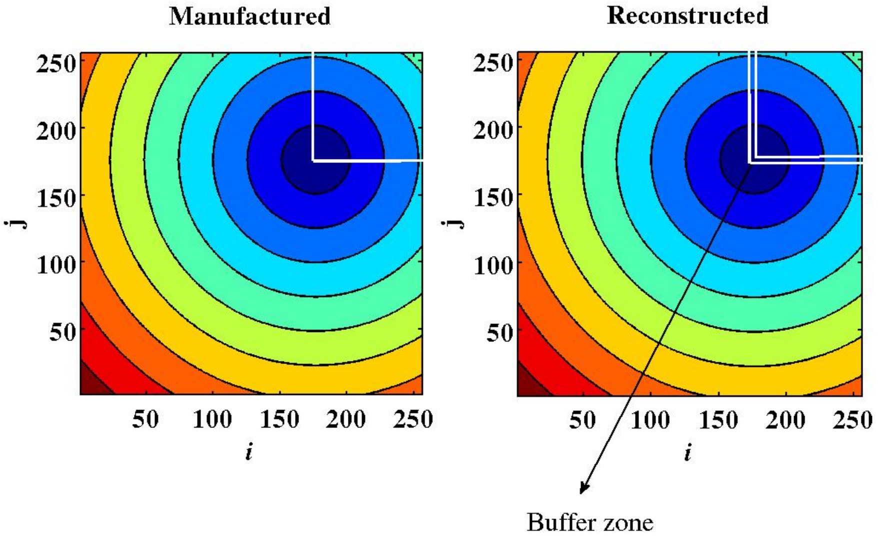

Figure 4: Contours of distance from the lower bottom corner of the white square is plotted using $d = \sqrt{(x - x_0)^2 + (y - y_0)^2}$ (left) everywhere in the domain without any special treatment to any cells (right) everywhere in the domain except the 3-cell wide single-sided buffer zone inside the white square using Eqs. (12) and (15). Grid indices are labeled on the horizontal and vertical axes.

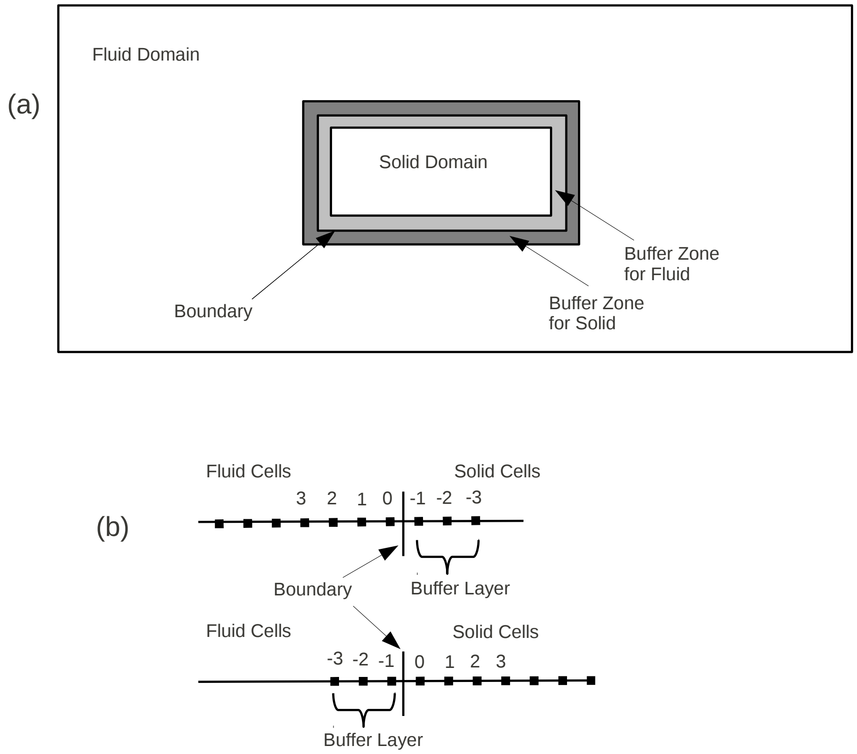

Figure 5: (a) Schematic of a Cartesian solid body inside a fluid domain; the shaded regions are 2-cell wide dual buffer zones for the solid and fluid domains (b) Cell-center indices for a one-dimensional grid marking the dual buffer zones.

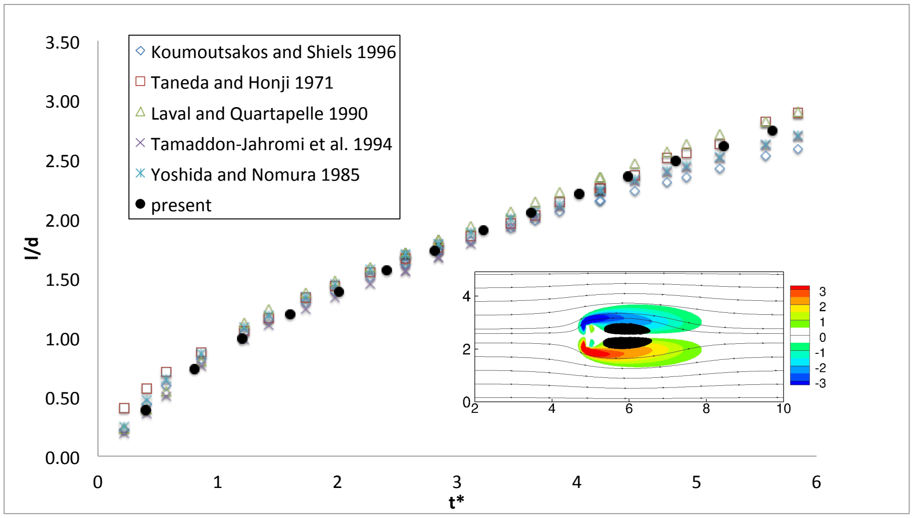

Figure 6: Experimental and numerical comparison of the recirculation zone growth for a case with an impulsively started thin vertical plate in a cross flow. References in the legend: [31, 33, 34, 35, 36]. Literature data is reproduced using Fig. 19 in [36]. A representative streamline pattern and colored non-dimensional vorticity contours at an intermediate time instant $t^* = 3.5$ is shown in the insert.

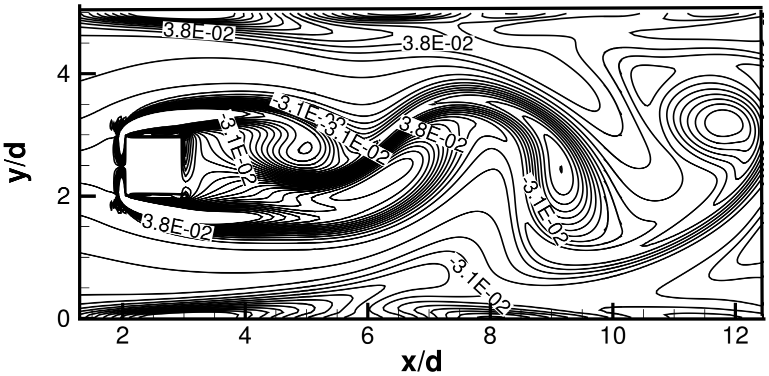

Figure 7: Instantaneous non-dimensional vorticity contours of an unsteady channel-confined cold flow around a square cylinder at $\mathrm{Re_d} = 100$ for a blockage ratio $d/H = 0.2$.

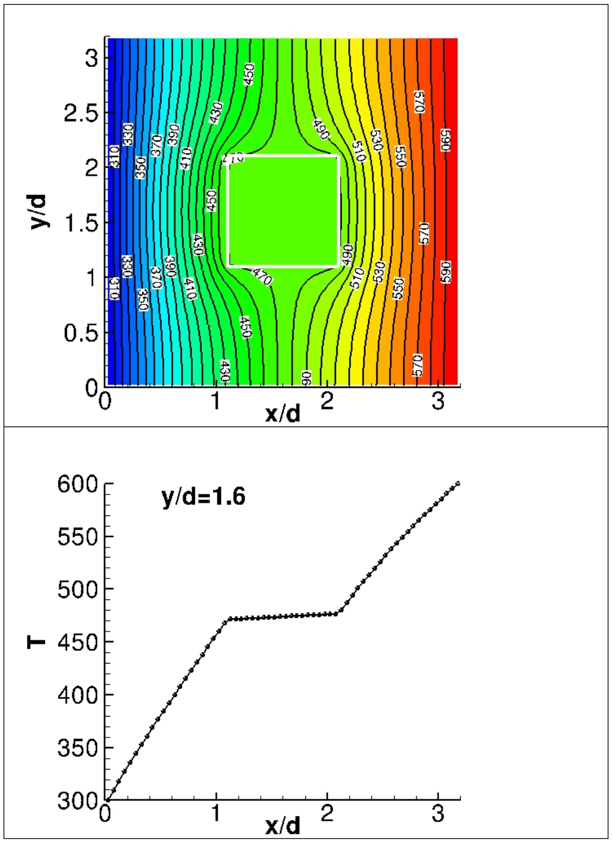

Figure 8: (top) Temperature contours at steady-state, white square marks the immersed ceramic solid object in stationary air (bottom) Temperature profile at $y/d = 1.6$.

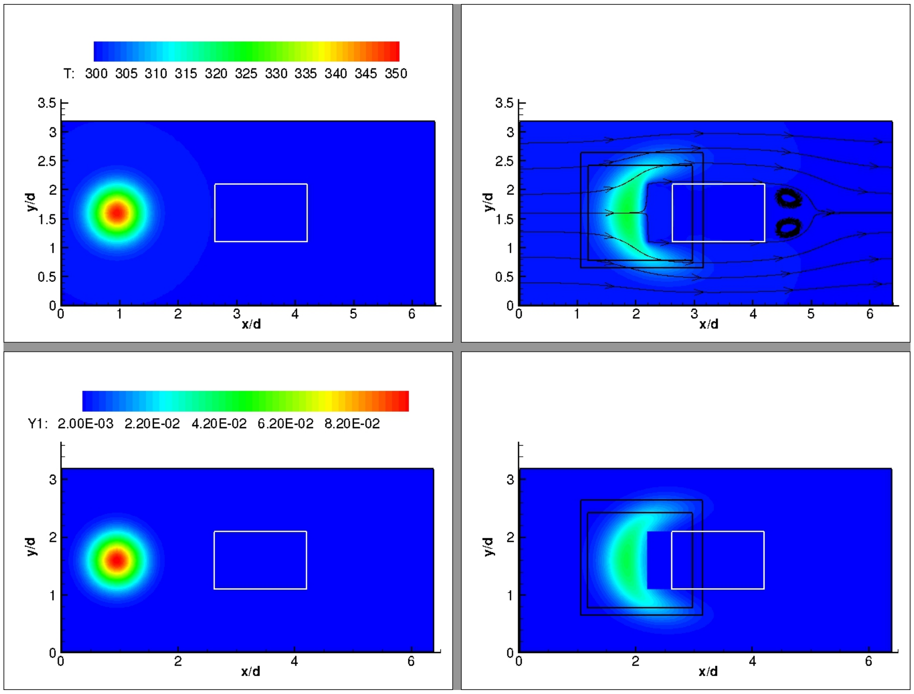

Figure 9: Contours of (top) T and (bottom) Y_{CH_4} at $t = 0$ (left column: initial condition for the SAMR convection-diffusion convergence test) and $t = 10$ms (right column). Rectangular solid is shown by white rectangle; level 1 and level 2 fine grid patches are marked by the black rectangles in the right column. Streamlines are overlaid on the T contours at $t = 10$ms.

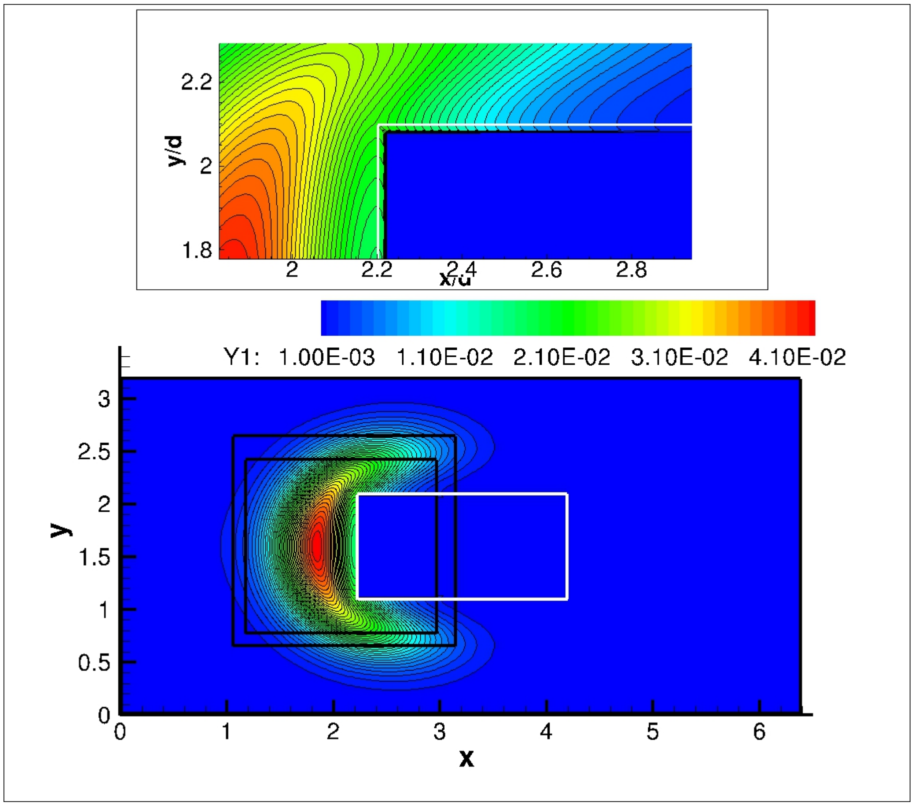

Figure 10: (top) Zoomed-in single-sided buffer zone for Y_{CH_4} (bottom) Fine grid patches overlaid on the Y_{CH_4} contours with the buffer-zone hidden.

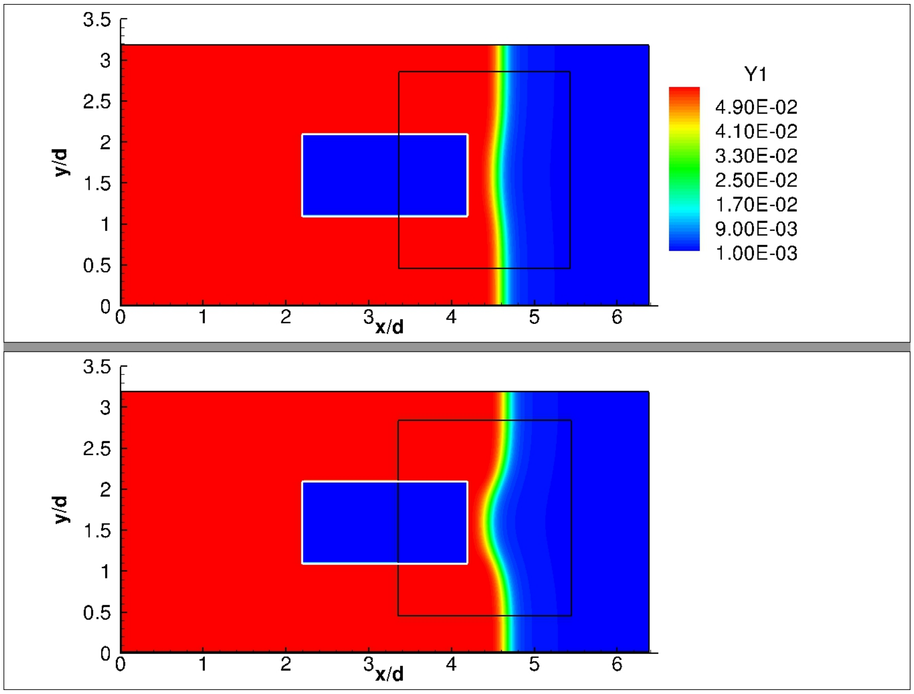

Figure 11: Fuel (Y_{CH_4}) contours for a premixed flame corresponding to a stoichiometric mixture interacting with a bluff-body (white rectangle) (top) initial condition corresponding to $t = 0$ (bottom) after $t = 1$ms. A level 1 fine grid patch is marked by the black rectangle.

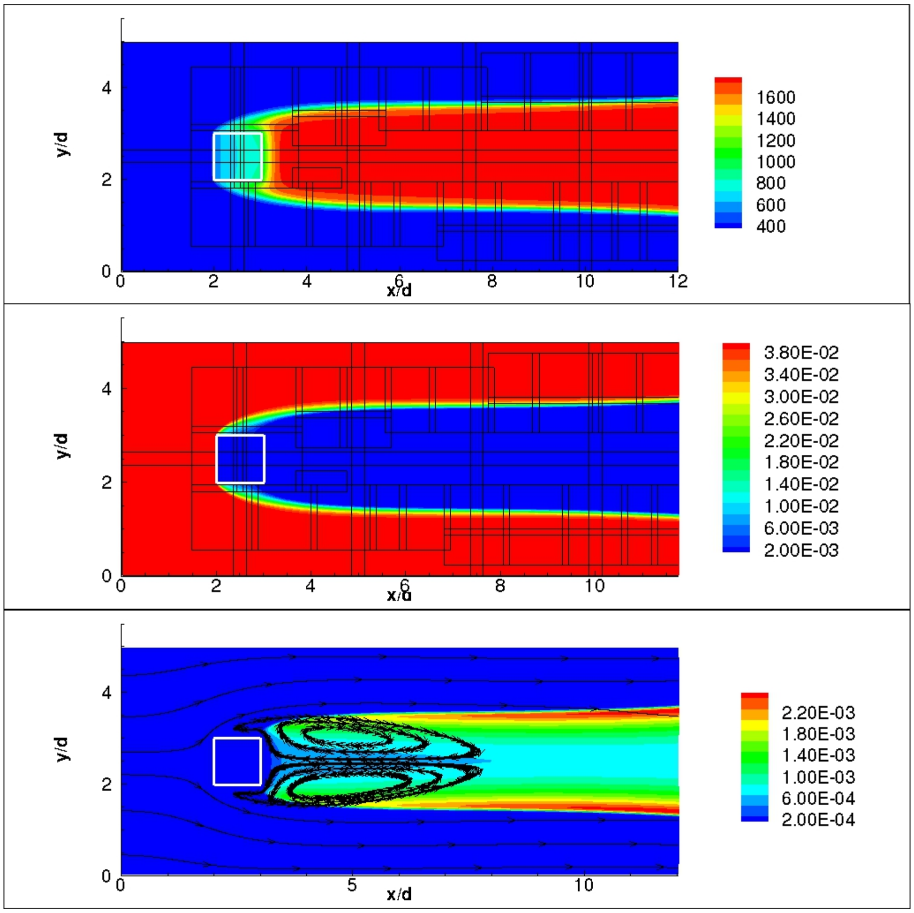

Figure 12: (top) Temperature contours with overlaid fine grid patches (middle) fuel Y_{CH_4} contours with overlaid fine grid patches (bottom) intermediate species Y_{OH} contours with overlaid streamlines of a reacting flow at equivalence ratio $\phi = 0.7$ around a confined rectangular cylinder at a flow $\mathrm{Re_d} = 1000$ for a blockage ratio $d/H = 0.2$.

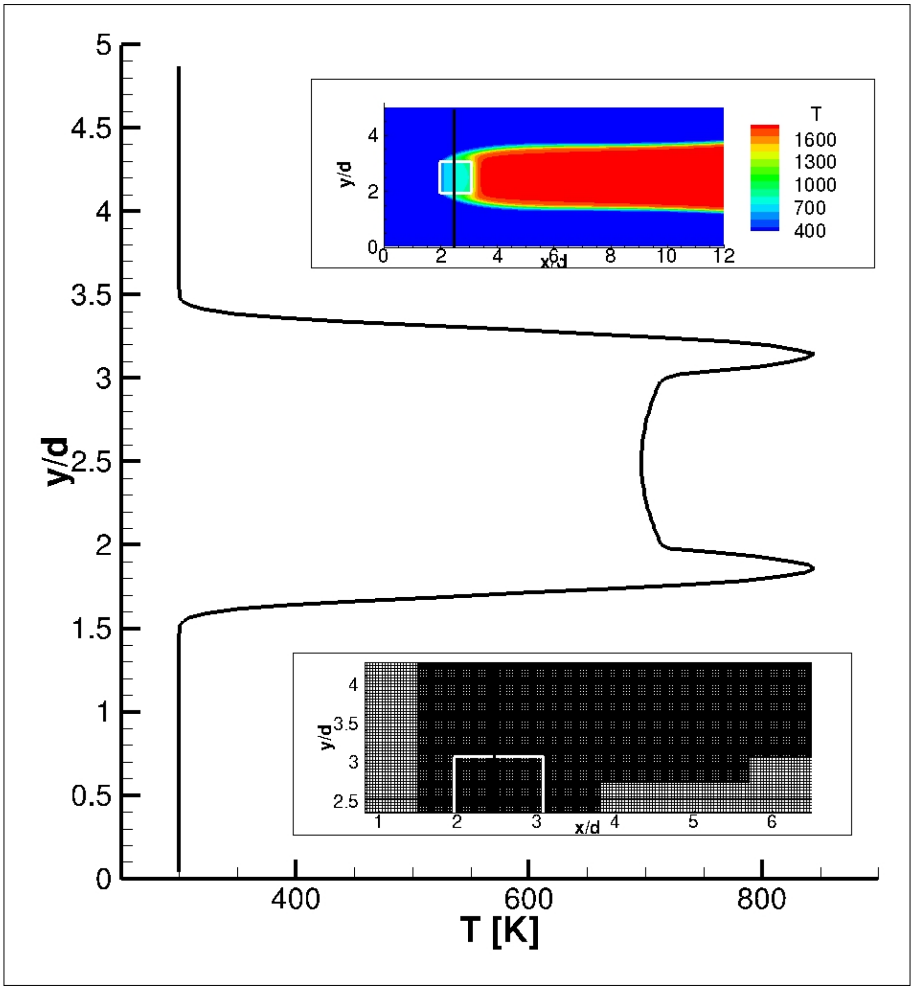

Figure 13: Temperature profile along $x/d = 2.5$ for a reacting flow at equivalence ratio $\phi = 0.7$ around a confined rectangular cylinder at a flow $\mathrm{Re_d} = 1000$ for a blockage ratio $d/H = 0.2$. Temperature contour with $x/d = 2.5$ location marked is shown in the top insert. Coarse and overlaid fine mesh is shown in a part of the computational domain in the bottom insert.